OPEN

GPS source solution of the 2004 Parkfield earthquake

N. Houlié[1,2,3], D. Dreger[1] & Kim, A.[4,5]

[1]Berkeley Seismological Laboratory - University of California, [2]ETH, SEG, Zurich, CH, [3]ETH, GGL, Zurich, CH, [4]Schlumberger, Cambridge, UK, [5]Graduate School of Nanobioscience, Yokohama City University, 22-2 Seto, Kanazawa-ku, Yokohama 236-0027, Japan.

We compute a series of finite-source parameter inversions of the fault rupture of the 2004 Parkfield earthquake based on 1 Hz GPS records only. We confirm that some of the co-seismic slip at shallow depth (<5 km) constrained by InSAR data processing results from early post-seismic deformation. We also show 1) that if located very close to the rupture, a GPS receiver can saturate while it remains possible to estimate the ground velocity (~1.2 *m/s*) near the fault, 2) that GPS waveforms inversions constrain that the slip distribution at depth even when GPS monuments are not located directly above the ruptured areas and 3) the slip distribution at depth from our best models agree with that recovered from strong motion data. The 95th percentile of the slip amplitudes for rupture velocities ranging from 2 to 5 km/s is ~55 ± 6 cm.

T oday, few instruments are able to constrain simultaneously the static and transient displacements for periods between 1 s to 1000 s or more. GPS is one of them. GPS is traditionally known to accurately measure distances and changes of distances through time if network measurements are repeated enabling the detection of surface ground motion including asymmetric deformation due to dislocation at depth[1,2], to constrain material property differences across faults[2–4], or to investigate the relationship between short- and long-term deformation of the continental lithosphere[5–9]. With improved telecommunications links and higher sampling rates, slip distribution models based on GPS data have become an important tool to study processes such as deformation transients from seismic wave propagation or directly from seismic rupture[10–29], changes in ionosphere status[30–35], volcanic plumes[36–38], water vapour delays[39], Early Warning systems[26,40,41] or more recently moment tensor analysis[42–44]. Constrained with GPS data or not, the dislocation amplitude (or fault slip) models occurring at depth during an earthquake are today the foundation of many geophysical studies including seismic hazard[45], rupture modelling[46], post- and inter- seismic deformation[47,48], stress transfer[9,49] or fault topography studies[50]. Meanwhile, the images of the co-seismic slip at depth of a given earthquake seem to depend on the imaging techniques and/or on the type of instrument used. Slip solutions based on static offsets (GPS or InSAR) define the extent of ruptured areas well but potentially incorporate signals from both co- and post-seismic deformation. Inversions of high frequency seismic records offer spatial detail but limits of ruptured fault segment is not well constrained or needs to be defined beforehand. In order to overcome the trade-off between resolution and rupture extent, many studies have tried to combine both static offsets and seismic waveforms in order to minimize the amount of post-seismic deformation to be included in the co-seismic slip model or/and to control the integration of seismic records[51,52–58]. Still, slip distributions vary among authors and processing methodologies[59] (see http://equake-rc.info/ for a extensive collection of fault rupture models for many earthquakes). This can be explained because, with such heterogeneity of instrumentation and sampling rates, the integration of seismic and geodetic data into a common model is not trivial, and the kinematic parameterization of such models is not unique. For example, if source functions are modelled as distributions of double-couples of forces distributed over the rupture area[60] for large events, other assumptions are commonly made in the setup of the inverse problem, such as the rheology and the velocity model, typically 1D, used to generate Green's functions, and inelastic or slow deformation (from rigid block motion to slow slip deformation) cannot be easily constrained by using seismic records only. An ideal setting would allow using both geodetic and seismic datasets as if they were equal in term of quality and use them under the same set of assumptions. To reach this level of confidence, we need to show that consistent slip models at depth can be retrieved using seismic and high-rate geodetic datasets with a same inversion algorithm. The fault system at Parkfield (Figure 1) is a relatively simple, approximately planer, near vertical fault. However, it is interesting to note that the approximate 20% velocity contrast attributed to the contact of the west side granites (faster) with the east side meta-sediments across the SAF[63], whereas for continental geology units maximum differences in elasticity parameters should not reach 30%, approximately
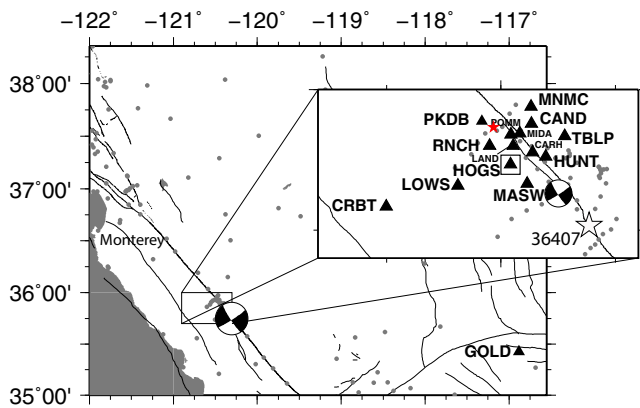
Figure 1 | The GPS and CSMIP strong-motion networks in California and near Parkfield. We locate the CSMIP sensors used in previous studies with small grey circles and GPS receivers with black triangles. The USGS Accelerometer (PHOB), collocated with the GPS site HOGS, is indicated by a white square. We show the location of the 1966 event (red star) and the focal mechanism provided by United States Geological Survey (USGS) for the 2004 Parkfield mainshock. The accelerograph (36407) and GPS site GOLD mentioned in the text are respectively highlighted by a solid-line star and black triangle.

Table 1 | Coseismic displacement at the Parkfield sites. No asymmetry of amplitude can be detected between the two sides of the fault

	Site	Lat. (deg.)	Lon. (deg.)	De (cm)	Dn (cm)	Dup (cm)
1	CAND	239.566	35.939	2.1	−4.2	−0.1
2	CARH	239.569	35.888	1.1	−1.2	−0.1
3	CRBT	239.249	35.791	−0.3	0.0	−0.1
4	HOGS	239.521	35.866	−2.2	3.5	−0.9
5	LAND	239.526	35.900	−3.3	3.0	−1.1
6	LOWS	239.406	35.829	−1.1	0.2	−0.2
7	MASW	239.557	35.833	−1.8	3.4	−1.3
8	MIDA	239.541	35.921	2.1	−4.5	−0.9
9	MNMC	239.566	35.970	0.5	−3.6	−0.8
10	POMM	239.521	35.919	−3.6	0.6	−0.5
11	PKDB	239.458	35.945	−3.4	0.9	0.8
12	RNCH	239.475	35.900	−2.8	1.8	0.2
13	TBLP	239.639	35.917	2.6	−1.8	0.9
14	HUNT	239.598	35.880	3.5	−3.5	0.4

10% in seismic wavespeed , (the maximal value for a oceanic-continental crust contact[3,4,61,62]). The 2004 Parkfield event is interesting because after a year the post-seismic surface deformation is larger than the co-seismic[64,65,84]. For this event, it is therefore critical to distinguish co-seismic and post-seismic deformation to better characterize the co-seismic rupture. We define as "co-seismic" any parameter changing during the first 30 s following the origin time of the event (T_0). The post-seismic period is defined as immediately following the co-seismic period. Finally, the density of the monitoring networks and their proximity to the epicenter (60+ seismic and geodetic instruments located within 250 km²) make of the 2004 Parkfield earthquake a very good dataset to test the capability of high-rate GPS in the near-field of large (M6+) earthquakes.

At the time of the event, the mini-Plate Boundary Observatory (PBO) GPS network maintained by United States Geological Survey (US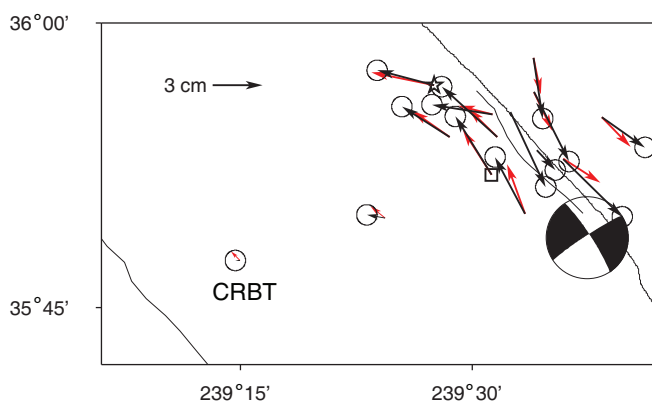GS), University of California at San Diego (UCSD) and University of California at Berkeley (UCB) was composed of 13 receivers recording data at 1 Hz (Figure 1) supplemented by one GPS site sampling data at 30 s (PKDB). The GPS site PKDB is co-located with a very-broadband seismic sensor PKD (STS-2) maintained by Berkeley Seismological Laboratory (BSL) of UCB. The mini-PBO GPS network was deployed around the epicenter of the 1966 Parkfield earthquake. At the time of the event, few GPS sites were located near the southern end of the Parkfield segment, near the location of the epicenter. Each monument was equipped with a ASHTECH Z-12 receiver with a Choke-Ring antenna. One GPS site (HOGS) was co-located with an accelerograph (PHOB) of the California Strong Motion Instrumentation Program (CSMIP) network (Figure 1).
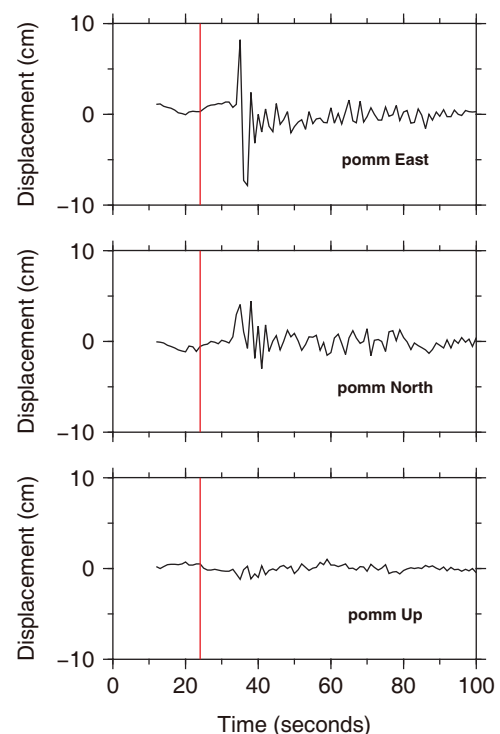

Figure 2 | Observed co-seismic displacements during the mainshock (black). The displacement at the CRBT site is less than 3 millimeters. The displacement observed at PKDB (star) indicates the rupture along the fault is limited to the south. All the displacement values are presented in Table 1. Co-seismic displacements have been inverted (red) using the OKINV software[1]. Minimum depth of the dislocation = 3.8 km, average slip = 49 cm. We indicate the focal mechanism provided by United State Geological Survey (USGS).

Figure 3 | Ground motion detected at the GPS site POMM with respect to the site CRBT. We indicate the origin time T_0 by using a red line.
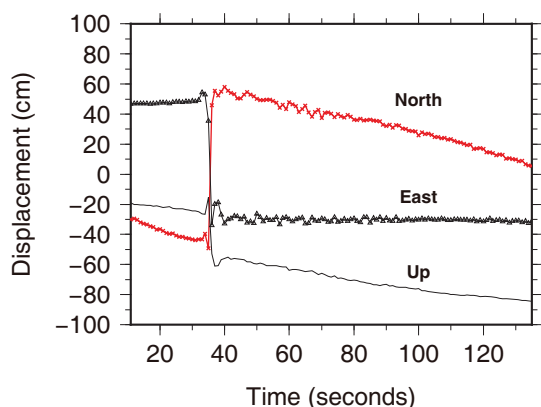
2

Figure 4 | Artifact of observation at the GPS site MIDA. During the rupture, GAMIT processing suggests the peak ground velocity is so high that it resulted in GPS receiver cycle-slip affecting the phase modeling.

Results

In order to constrain the amplitude of the surface deformation history during the first days following the earthquake as suggested by Langbein et al.[84], we processed the 30s sampling rate data using the GAMIT 10.4 tool suite[66]. The maximum static displacement at the surface is equal to ~5 cm (Figure 2). As expected[67], we find that the displacement of the site GOLD (located 200 km south-west of Parkfield, Figure 1) during the earthquake can be neglected and that the motion of the site CRBT is less than 2 mm (Figure 2). Daily time-series of displacement display a non-linear temporal evolution of the surface deformation during the days and weeks immediately following the mainshock[64,67]. We inverted for the average slip motion at depth for data collected during the first day that followed the earthquake computing the effect at the surface of a buried dislocation in a purely elastic half-space[68] using the nonlinear inversion algorithm OKINV 3.16[1,69]. In order to avoid reaching a local minimum solution, we use 200 Monte-Carlo starts. The inverted solution corresponds to an averaged co-seismic slip at depth of 20 cm. The surface velocity field (Table 1) is shown in Figure 2. The data inversion using 24 h of data implies larger surface displacement than those inferred from the GPS solutions using 20 minutes GPS data[53] suggesting that post-seismic deformation was already on-going during the first 24 h following the earthquake. An inversion of the difference of motion between the two long-term GPS datasets suggests an asymmetry of motion with a fault plane solution shifted to the east with respect to the San Andreas fault (SAF) trace at the surface. This result implies that the elastic response to the rupture during the hours following was asymmetric and/or some post-seismic deformation happened very quickly after the end the earthquake rupture and/or the co-seismic ground motion was asymmetric (the southwestern block moved less than the northern one).

We describe here how the GPS 1 Hz residuals have been processed. This approach has already been used to detect atmosphere disturbances caused by atmospheric volcanic explosions[36,37] or seismic wave propagation in the far field[23]. First, we processed all 1 Hz GPS data available (13 sites) using GAMIT 10.4[66]. We then extracted the LC phase residuals for which the ionosphere contribution has been minimized. At this stage, with phase cycle ambiguities being fixed, clock drifts removed (double differences have been applied) and with troposphere, ionosphere or tide changes being insignificant to the waveform shapes over the first 30 s following the start of the event, phase residuals only highlight the deformation of the network. Each phase residual correspond indeed to the dot product of the ground displacement with the unit vector defined by the Line-Of-Sight (LOS) between a site and a satellite. All single-difference phase residuals available for a given site are inverted in order to retrieve the motion in the local reference frame (East, North and Vertical). Waveforms are 30-seconds long Figure 3 and include 10 seconds of data before the origin time (17:15:24 UTC). To remove any common mode translation of the network, we subtract the motion history of the site CRBT (from now on fixed) to each waveform in the dataset. We compare the GPS displacement waveforms (GPS site HOGS) with acceleration data (converted into displacement) recorded by collocated instruments (PHOB strong motion sensor). In order to compute displacement from acceleration, we corrected the raw accelerograms of the instrument responses and decimated the data to 1 Hz using the SAC2000 software[70]. Filtered strong motion displacement time series exhibit a long-period parabolic drift as expected[71]. In order to remove this artefact of integration, we use a Butterworth filter[72] to high-pass (T = 50 s) the displacement time-series computed from accelerograms. We find that both waveform datasets are in agreement (Figure A2) and conclude that even if GPS and accelerometer instruments have very different designs, inversion of both dataset if sampled at the same frequencies and have the same applied filters should lead to similar models. We focus now on the other waveforms recorded by GPS receivers that are not collocated with seismic instruments. All GPS waveforms final offsets match the expected static offsets except for those computed for the site MIDA. Indeed, the final offset of the GPS site MIDA is close to ~120 cm (Figure 4). We refer to this value as the dynamic offset of MIDA
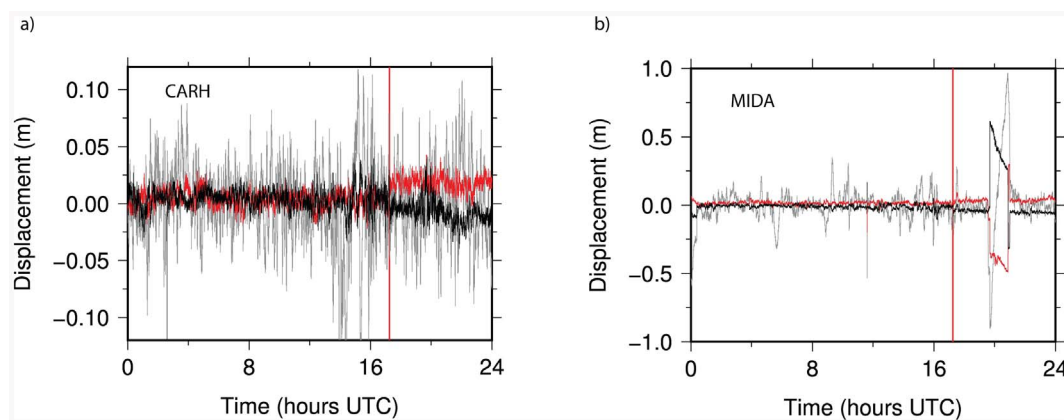

Figure 5 | Variations of the baseline length components between the sites a) CRBT-CARH and b) CRBT-MIDA. CRBT is fixed during the processing. East, North and Vertical components are respectively indicated by using red, black and grey lines. The origin time is indicated by a red vertical line. We conclude that the TRACK software could not reproduce the cycle slip shown in Figure 4. Therefore, we exclude the possibility of an internal receiver problem.
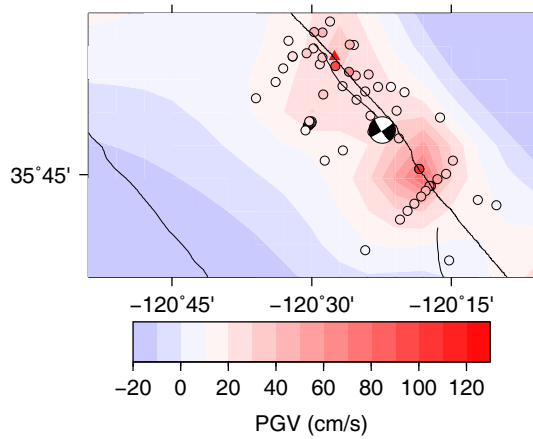
Figure 6 | Peak Ground Velocity map compared with the maximum ground velocity measured at MIDA (triangle). The PGV values obtained from the COSMOS virtual data center (http://db.cosmos-eq.org) have been interpolated using the *surface* function of Generic Mapping Tools on a 5-km interval grid.

($d_{dynamics}$). In order to check whether this motion to be related to a software issue, we processed the same data (baseline CRBT-MIDA) by using the software TRACK and did not observe the same processing artefact (Figure 5). To explain such discrepancies, we argue that the rapid carrier phase change at a unique location of the network could not be modelled by using the smooth phase function applied by

GAMIT across the GPS network. On the contrary, TRACK's processing strategy, which is based on the phase difference modelling between two sites (assuming one of them is not moving, an assumption that is not true in this case), is more flexible and because ambiguities were fixed properly after the phase slip, the phase change was only an artefact of measurement. We think this artefact is the first GPS clip (or earthquake induced cycle slip) ever observed. As such motion could correspond to a M7+ rupture reaching the surface, unconstrained cycle slips could lead to significant misleading alert for Earthquake Early Warning or detection alert systems[40,41,73] supplemented by the tracking of GPS sites positions. However, we can still use the capability of GPS to clip to calculate the maximum ground motion. Indeed, if we hypothesize that the rapid motion of the site MIDA between two epochs (one second) induced a cycle slip of an unknown number n of carrier cycles and the dynamic offset ($d_{dynamics}$) is almost equal the static offset d_{static} (itself smaller than a phase cycle length), we can retrieve the number of carrier cycle n that slipped during one second by solving the following system of equations:

$$d_{true} \sim d_{dynamics} n \times \lambda_{LC} + \epsilon_1 \qquad (1)$$

$$d_{true} \sim d_{static} + \epsilon_2 \qquad (2)$$

Where λ_{LC}, the wavelength of the ionosphere-free LC carrier equals 24 cm. The true phase change remains unknown because the phase change artefact cannot only be represented by full phase cycles. ϵ_1 represents this uncertainty. We take that ϵ_1 is close to the uncertainty on the GPS carriers phase (2 mm). ϵ_2 represents the post-seismic
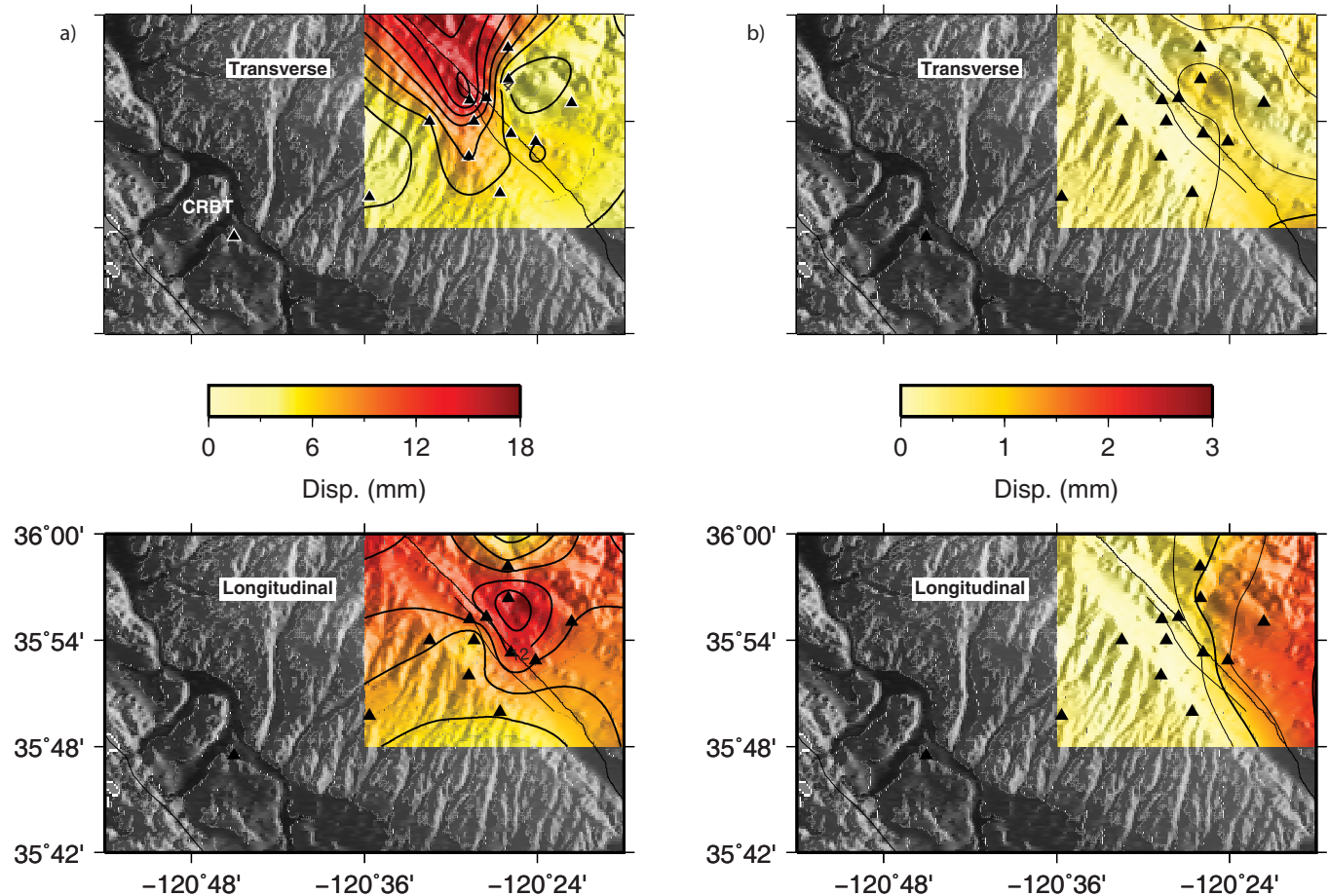

Figure 7 | Maximum displacement (a) during the rupture propagation compared to static final offsets (b). We find that both the peak-to-peak amplitudes and the static displacements are ~60% larger on the eastern side of SAF.
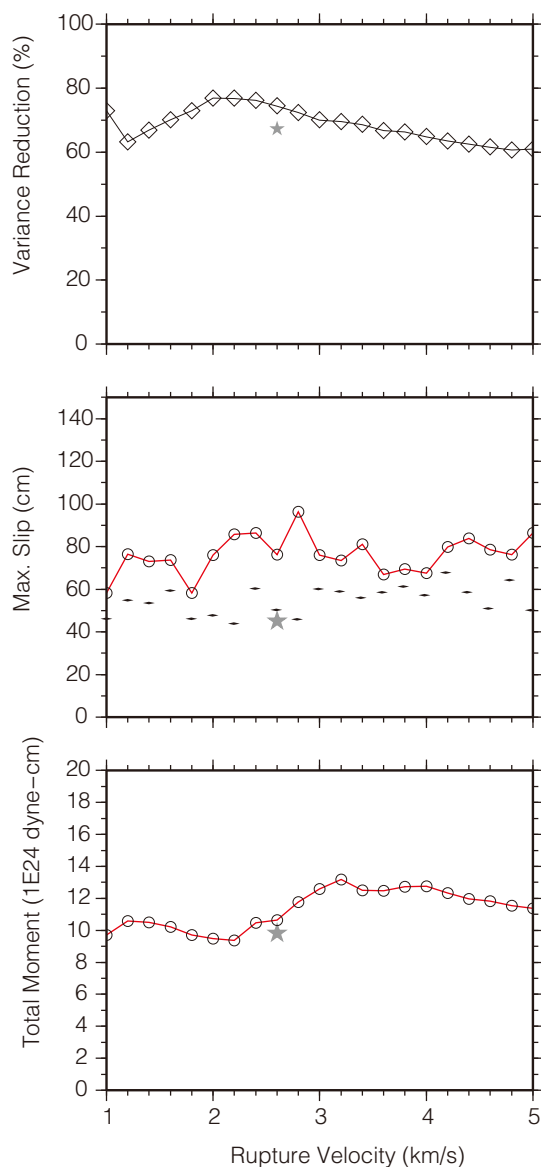
Figure 8 | (a) Inversion output parameters of the GPS time-series for various rupture velocities (RV) for symmetric velocity models. The best solution proposed by[53], is indicated by a gray star. 95th percentile slip amplitude are indicated by black diamonds. For rupture velocities (RV) between 2.0 and 3.0 km/s, maximum slip is 55 cm.

deformation that occurred during a day, and to be equal or less than ϵ_1. The motion (d_{static}) of MIDA is ~5 centimeters (Table 1), we estimate the number of cycles n to be removed of the original time-series to be 5 (~1.2 m). As this motion is completed within a second, we reach the conclusion that the ground velocity at MIDA was close to 1.2 m/s. Such a motion rate is compatible with the Peak Ground Velocity (PGV) observed at the strong-motion seismic site 36407 (located very south of MIDA but within the fault zone at 120.307 W, 35.758 N, 24 km SE from the GPS site MIDA, with PGV = 1.05 m/s). All PGV are presented in Figure 6. Because we do not want to introduce biases in the slip models, we reprocessed the 1 Hz displacement time-series after excluding the site MIDA.

The 1 Hz GPS time-series show well defined seismic first arrivals and for some sites, nonzero offsets at the end of their displacement history. We find that the motion of the sites located on the eastern side of the SAF is up to 60% larger than the motion of the sites located on the other side of the fault (Figure 7). The asymmetric character of

the rupture confirms the observation made with daily displacement time-series. This asymmetry of motion could be due to a limited number of parameters. The first one would be the variation of rheology in the direction perpendicular to the fault. Others could be 1) that the fault plane is not perfectly vertical at depth[50,74] or the velocity model should be different across the fault, which has been tested in previous studies[52,53,75]. It is difficult argue for any one hypothesis. It is clear that the velocity contrast exists from tomographic analysis, and that the fault plane is not perfectly vertical[85]. Thus the third possibility, that there could be anisotropic rheological properties, must be considered only if after accounting for velocity model differences across the fault, 3D structure, and non-vertical fault dip, taking into account the associated uncertainties, still results in a significant residual.

We successfully inverted the GPS waveforms (low-pass filtered at T = 3 s) of 9 of the 13 (CAND, CRBT, HOGS, HUNT, LAND, LOWS, MASW, RNCH, TBLP) high-sampling rate sites using the approach defined by[60,76] for rupture velocities (RV) ranging from 1.0 to 5 km/s (Figure 8). Our filtering options fits with those used by *Kim and Dreger* (2008) in their study (low-pass filter at T = 2 s). Four sites were dominated by either near-field 3D effect(s) that could not be modelled using a smooth 1D velocity profile (CARH, POMM, MNMC) and/or clipping (MIDA). We used a set of Green's function based on the 1D seismic model GIL7[77]. Green's functions (different from those used by Kim and Dreger, 2008) were designed to render both seismic wave arrivals and the static offsets for data collected in the very near field. The variance reduction for the various models is always larger than 60%. The total moment release estimates are between 9 and $14{\times}10^{24}$ dyne.cm (Figure 8). The slip pattern is stable for various rupture velocities except toward the southern end of the rupture where coverage is poor. We show that waveform fits are good for solutions with rupture velocities between 2 to 3 km/s (Figure 9). The same work detailed below has been completed using an asymmetric model[78] without improving the inversion variance reduction or changing the shape of slip distribution at depth (Supplementary Materials Figures B3, B4 and B5 are displaying these results). The computed slip distribution solutions (Figure 10) also fit well the spatial slip distribution inferred from the accelerometer records[53]. However, the top 5 percent of the slip values exceed (up to 125 cm) the maximum slip values (50 cm) constrained by other techniques (Table 2). However, the 95th percentile does not vary significantly with rupture velocity (Figure 8) with a maximum slip amplitude inferior to 67 cm. The peak slip area is close to the epicenter locations of the 1966 Parkfield mainshock and of the high-frequency 2004 Parkfield secondary event[79]. An area of low slip (10 cm or less) between the 1966 and the 2004 hypocenters is visible as for other models[53,80]. We expect that the slip to be poorly constrained near the southern end of the fault (epicentre area) where the GPS network is sparse at the time of the rupture. Bootstrap inversion tests (see in particular slip models MH and MV in Supplementary Materials) show that the slip amplitudes near the hypocenter are, in fact, constrained by the horizontal components. The slip model constrained by GPS compares visually well with other slip models based on strong motion data[52] computed with a different algorithm. The differences between strong motion model[53] computed using the same software are limited between −10 and +10 cm. This value fits well with standard deviation for slip proposed by *Page et al.*, (2009). We therefore assume that 10 cm as the 1σ uncertainty on the slip, and we therefore are not able to detect significant difference between our model and the one proposed by *Kim and Dreger*, (2008) at the southern end of the fault. We then compare the slip distribution inferred from the inversion of our GPS waveforms (RV = 2.2 km/s, and RV = 2.6 km/s) with a slip model inferred from SAR interferometry (InSAR)[80]. We find discrepancies on the slip amplitude above the 5 km depth along the northern part of the Parkfield segment (Figures 10 and 11, as suggested for the first 24 hours by *Johnson*
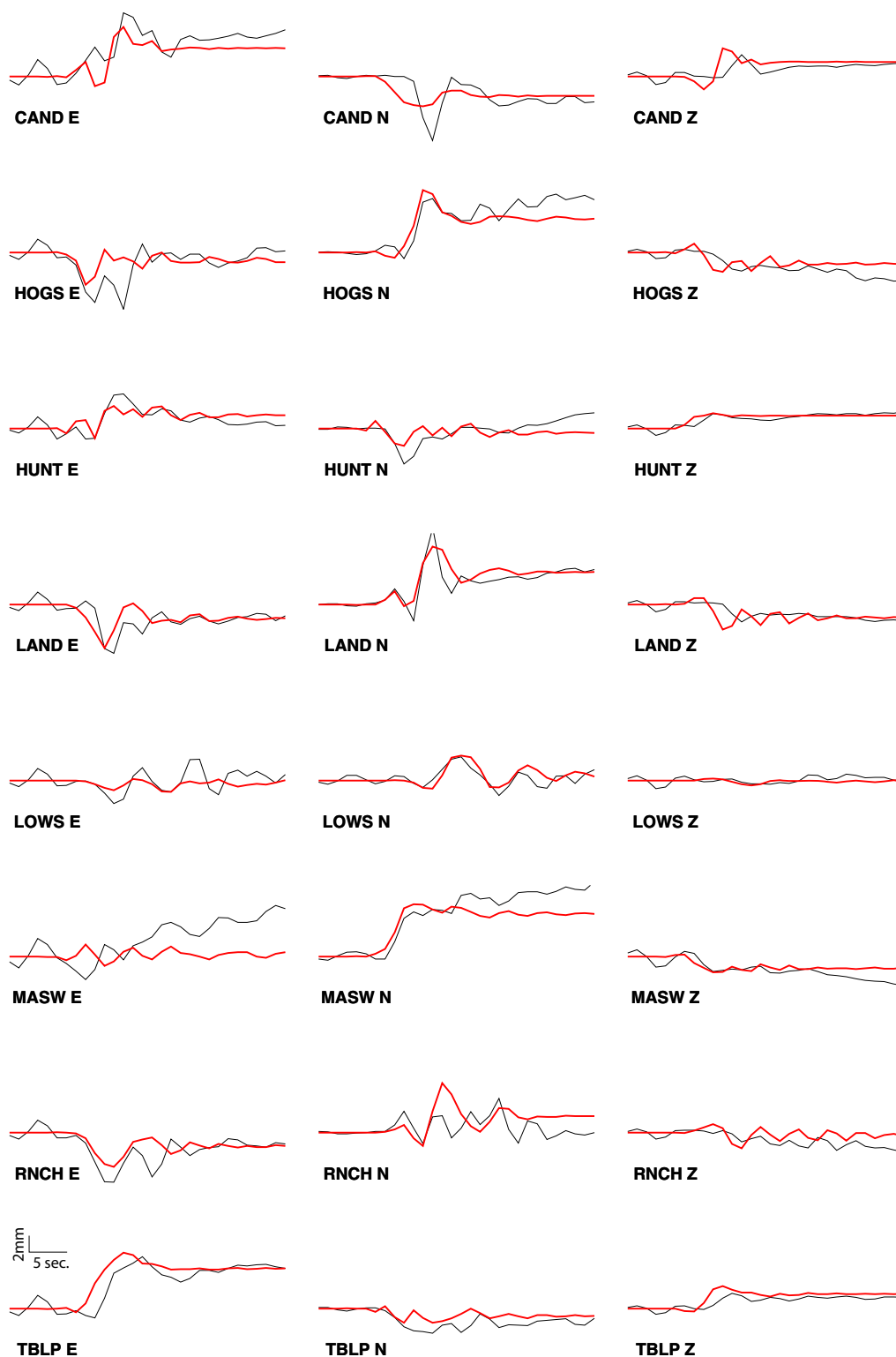
Figure 9 | Fit between the GPS waveforms (black) and the model (red) for RV = 2.6 km/s.

et al., (2006). As the resolution of InSAR is close to ±2 mm/yr for best configurations[62], and we showed that the near-surface slip must be well constrained (see section) near the surface if measurement points are densely distributed at the surface. We conclude this sub-surface slip is real but not co-seismic. Other slip models based on daily GPS solutions confirm this hypothesis[65]. The concentration of microseismicity at shallow depth during the days following the main-shock also supports this hypothesis[81] (Figure 11).

Discussion

The spatial distribution of the GPS network was not optimal at the time of the Parkfield earthquake. Today, the sensitivity of the con-tinuous GPS network, after the deployment of the PBO GPS network would allow a better description of slip at all depth. The radiated energy from the first asperity is concentrated in higher frequency[53] which explains that 1 Hz GPS time-series could not constrain slip near the epicenter regardless of the good sensitivity of the GPS hori-
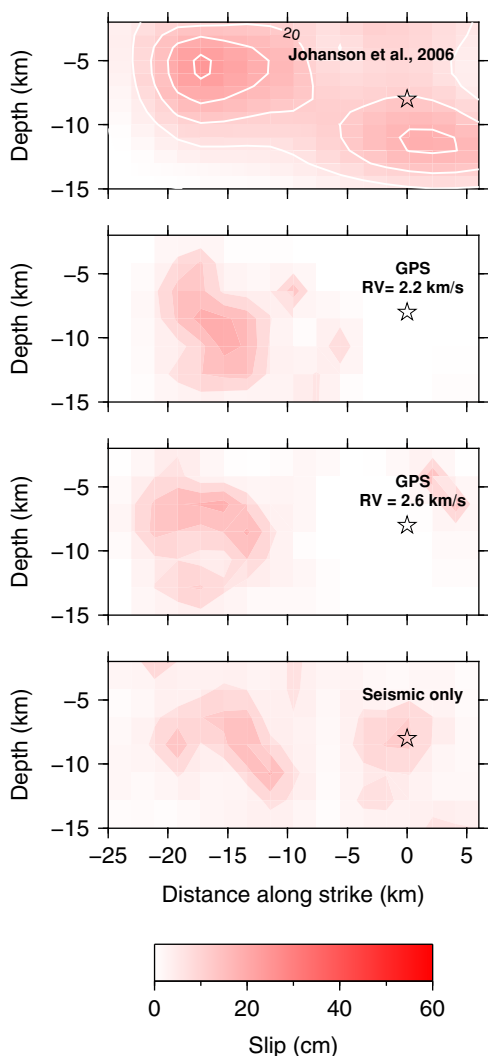
Figure 10 | Slip distribution from various datasets. We note that the GPS models are able to map the slip distribution as well as the seismic solutions. The slip to the southern tip of the fault is not well constrained likely because the GPS network was not deployed above the 2004 hypocenter. Models from Johanson et al., 2006 (white contour lines every 10 cm) and Kim and Dreger, 2008 are models inferred using InSAR and Strong-motion data only.

zontal components. Along the northern part of the Parkfield segment, we retrieved a slip model at depth that is similar to those obtained from seismic records with a new set of Green's functions and/or different inversion algorithms. This implies that inversion input parameters do not drive the slip model characteristics. The mapping of slip at depth allows us concluding that the post-seismic slip locations coincides with areas where the aftershocks occurred during the 2 days following the mainshock at least along the northern section of the SAF at Parkfield (Figure 11). The comparison of our
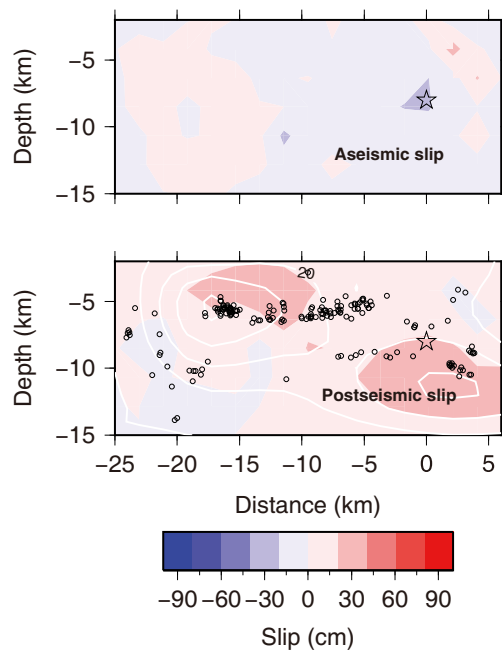

Figure 11 | Aseismic (top) and Postseismic (bottom) slip distributions. We subtracted the GPS dynamic solution (RV = 2.6 km/s) to the seismic and InSAR slip solution. We note that apart of the overestimation of slip in the area of the peak slip, all the late slip is concentrated between the surface and 5 km depth, or in an area surrounding the actual hypocenter of the source and in the zone between the 1966 and the 2004 hypocenter areas. We note that the area where post-seismic slip occurs coincides with the location of micro-earthquakes happening between the Parkfield mainshock and the second SAR acquisition ($\sim T_0 + 2$ days). The InSAR model discussed in the text is indicated by using white line contours (a line every 10 cm).

models with the model obtained from InSAR[80] confirm that post-seismic slip in the 0 to 5 km depth range initiated minutes after the end of the mainshock. This suggest the surface fractures mapped within the fault zone[82] were not co-seismic, but were instead created by post-seismic processes following the mainshock[83].

Methods

Beyond the challenge of what is an optimum network geometry for recovery of coseismic slip using only GPS data, there remains, the question of the depth sensitivity of GPS observations to slip at depth. To examine this we model rectangular dislocations of various depth extent for two GPS networks at Parkfield: the GPS network as it was in place in September 2004 and today's GPS network (including the newest PBO sites). The dislocation's slip amplitudes range from 10 to 50 cm (the maximum displacement) for 3 sources rupturing the entire length (25 km) of the SAF segment: from 0 to 5 km, 5 to 10 km and 10 to 15 km (Figure A1). We find that in 2004, the GPS network would not be able to detect displacement if the slip was smaller than 20 cm and shallower than 5 km (Figure A1). The addition of InSAR to the GPS data is therefore necessary to quantify accurately the early postseismic deformation that occurred near the surface. The addition of Plate Boundary Observatory (PBO) sites since 2004–2005 allowed increasing the number of short baselines, and decreased the minimal baseline length; two improvements allowing leading to better resolution of the shallow deformation near the fault.

Table 2 | Statistics of the models for various instrumentations. We note while the variance reductions (Var.) are similar the time span range from seconds to days. Rupture Velocities (R. V.) are indicated when relevant

Instr.	Time span (s) (s)	Var.	R.V. (km/s)	Mean slip (cm)	$\pm 1\sigma$	Ref.
InSAR	$\sim 1.5\ 10^5$	90%	N/A	12.0	11.12	*Johanson et al., 2006*
Accelerograph	30	60%	2.6	5.6	7.8	*Kim and Dreger, 2008*

1. Clarke, P. *et al.* Geodetic investigation of the 13 May 1995 Kozani-Grevena (Greece) earthquake. *Geophys. Res. Lett.* **24**, 707–710 (1997).

2. Freymueller, J. T., Murray, M., Segall, P. & Castillo, D. Kinematics of the pacific-north america plate boundary zone, northern california. *J. Geophys. Res.* **104**, 7419–7441 (1999).

3. Fulton, P., Schmalzle, G., Harris, R. & Dixon, T. Reconciling patterns of interseismic strain accumulation with thermal observations across the Carrizo segment of the San Andreas Fault. *Earth Planet. Sci. Lett.* **300**, 402–406 (2010).

4. Houlié, N. & Romanowicz, B. Asymmetric deformation across the San Francisco Bay Area faults from GPS observations in Northern California. *Phys. Earth Planet. Inter.* **184**, 143–153 (2011).

5. Bourne, S. J. *et al.* Crustal deformation of the marlborough fault zone in the south island of new zealand: Geodetic constraints over the interval 19821994. *J. Geophys. Res.* **103**, 30147–30165 (1998).

6. Holt, W. E. Correlated crust and mantle strain fields in Tibet. *Geology* **28**, 67–70 (2000).

7. Kreemer, C. Absolute plate motions constrained by shear wave splitting orientations with implications for hotspot motions and mantle flow. *J. Geophys. Res.* **114**, 1–18 (2009).

8. Houlié, N. & Stern, T. A comparison of GPS solutions for strain and SKS fast directions: Implications for modes of shear in the mantle of a plate boundary zone. *Earth Planet. Sci. Lett.* **345–348**, 117–125 (2012).

9. Houlié, N. & Phillips, R. Quaternary rupture behavior of the Karakoram Fault and its relation to the dynamics of the continental lithosphere, NW Himalaya Western Tibet. *Tectonophysics* **599**, 1–7 (2013).

10. Larson, K. *et al.* Volcano monitoring using the Global Positioning System: Filtering strategies. *J. Geophys. Res.* **106**, 19453–19464 (2001).

11. Bock, Y., Prawirodirdjo, L. & Melbourne, T. Detection of arbitrary large dynamic ground motions with a dense high-rate GPS network. *Geophys. Res. Lett.* **31**, 1–4 (2004).

12. Ji, C., Larson, K., Tan, Y., Hudnut, K. & Choi, K. Slip history of the 2003 San Simeon earthquake constrained by combining 1-Hz GPS, strong motion, and teleseismic data. *Geophys. Res. Lett.* **31**, 1–4 (2004).

13. Miyazaki, S. *et al.* Modeling the rupture process of the 2003 September 25 Tokachi-Oki (Hokkaido) earthquake using 1-Hz GPS data. *Geophys. Res. Lett.* **31**, 1–4 (2004).

14. Blewitt, G. *et al.* Rapid determination of Earthquake magnitude using GPS for Tsunami Warning Systems. *Geophys. Res. Lett.* **33**, 1–4 (2006).

15. Kobayasji, R., Miyazaki, S. & Keketsu, K. Source processes of the 2005 West Off Fukuoka Prefecture earthquake and its largest aftershock inferred from strong motion and 1-Hz GPS data. *Earth Planets Space* **58**, 57–62 (2006).

16. Ohta, Y., Meiano, I., Sagiya, T., Kimata, F. & Hirahara, K. Large surface wave of the 2004 Sumatra-Andaman earthquake captured by the very long baseline kinematic analysis of 1-Hz GPS data. *Earth Planets Space* **58**, 153–157 (2006).

17. Emore, G., Haase, J., Choi, K., Larson, K. & Yamagiwa, A. Recovering absolute seismic displacements through combined use of 1-Hz GPS and strong motion accelerometers. *Bull. Seismol. Soc. Am.* **97**, 357–378 (2007).

18. Wang, G., Boore, D. M., Tang, G. & Zhou, X. Comparisons of ground motions from collocated and closely spaced one-sample-per-second Global Positioning System and accelerograph recordings of the 2003 M 6.5 San Simeon, California, earthquake in the Parkfield Region. *Bull. Seismol. Soc. Am.* **97**, 76–90 (2007).

19. Yokota, Y., Koketsu, K., Hikima, K. & Miyazaki, S. Ability of 1-Hz GPS data to infer the source process of a medium-sized earthquake: The case of the 2008 Iwate-Miyagi Nairiku, Japan, earthquake. *Geophys. Res. Lett.* **36**, 1–4 (2009).

20. Delouis, B., Nocquet, J.-M. & Vallée, M. Slip distribution of the February 27, 2010 Mw = 8.8 Maule Earthquake, central Chile, from static and high-rate GPS, InSAR, and broadband teleseismic data. *Geophys. Res. Lett.* **37**, 1–4 (2010).

21. Bock, Y., Melgar, D. & Crowell, B. Real-Time Strong-Motion Broadband Displacements from Collocated GPS and Accelerometers. *Bull. Seismol. Soc. Am.* **101**, 2904–2925 (2011).

22. Avallone, A. *et al.* Very high rate (10 Hz) GPS seismology for moderate-magnitude earthquakes: The case of the Mw 6.3 L'Aquila (central Italy) event. *J. Geophys. Res.* **116**, 1–14 (2011).

23. Houlié, N., Occhipinti, G., Shapiro, N., Lognonné, P. & Murakami, M. New approach to detect seismic surface waves in 1 Hz-sampled GPS time series. *Sci. Rep.* **1**, 1–10 (2011).

24. Ohta, Y. *et al.* Quasi real-time fault model estimation for near-field tsunami forecasting based on RTK-GPS analysis: Application to the 2011 Tohoku-Oki earthquake (Mw 9.0). *J. Geophys. Res.* **117**, 1–16 (2012).

25. Mitsui, Y. & Heki, K. Observation of Earth's free oscillation by dense GPS array: After the 2011 Tohoku megathrust earthquake. *Sci. Rep.* **2**, 1–4 (2012).

26. Wright, T., Houlié, N., Hildyard, M. & Iwabuchi, T. Real-time, reliable magnitudes for large earthquakes from 1 Hz GPS precise point positioning: the 2011Tohoku-Oki (Japan) earthquake. *Geophys. Res. Lett.* **39**, 1–5 (2012).

27. Meng, G. *et al.* Coseismic Deformation of the 2010 Mw 6.9 Yushu Earthquake Derived from GPS Data. *Seis. Res. Lett.* **84**, 57–64 (2013).

28. Guo, A. *et al.* Observation of Core Phase ScS from the Mw 9.0 Tohoku?Oki Earthquake with High-Rate GPS. *Seis. Res. Lett.* **84**, 594–599 (2013).

29. Melgar, D., Crowell, B., Bock, Y. & Haase, J. Rapid modeling of the 2011 Mw 9.0 Tohoku-oki earthquake with seismogeodesy. *Geophys. Res. Lett.* **40**, 2963–2968 (2013).

30. Ducic, V., Artru, J. & Lognonné, P. Ionospheric remote sensing of the Denali Earthquake Rayleigh surface waves. *Geophys. Res. Lett.* **30**, 1–4 (2003).

31. Mai, C.-L. & Kiang, J.-F. Modeling of ionospheric perturbation by 2004 Sumatra tsunami. *Radio Sci.* **44**, 1–17 (2009).

32. Karia, S. & Pathak, K. Change in refractivity of the atmosphere and large variation in TEC associated with some earthquakes, observed from GPS receiver. *Adv. Space Res.* **47**, 867–876 (2011).

33. Galvan, D. A., Komjathy, A., Hickey, M. P. & Mannucci, A. J. The 2009 samoa and 2010 chile tsunamis as observed in the ionosphere using gps total electron content. *J. Geophys. Res.* **116**, 2156–2202 (2011).

34. Galvan, D. A. *et al.* Ionospheric signatures of Tohoku-Oki tsunami of March 11, 2011: Model comparisons near the epicenter. *Radio Sci.* **47**, 1–10 (2012).

35. Komjathy, A. *et al.* Detecting ionospheric TEC perturbations caused by natural hazards using a global network of GPS receivers: The Tohoku case study. *Earth Planets Space* **64**, 1287–1294 (2012).

36. Houlié, N., Briole, P., Nercessian, A. & Murakami, M. Sounding the plume of the 18 August 2000 eruption of Miyakejima volcano (Japan) using GPS. *Geophys. Res. Lett.* **32**, 1–4 (2005).

37. Houlié, N., Briole, P. & Nercessian, A. 2005, March 9th Mount St Helens explosion. *EOS Trans. Am. Geophys. Union* **86**, 277–284 (2005).

38. Larson, K. A new way to detect volcanic plumes. *Geophys. Res. Lett.* **40**, 2657–2660 (2013).

39. de Haan, S., Holleman, I. & Holtslag, A. Real-Time Water Vapor Maps from a GPS Surface Network: Construction, Validation, and Applications. *J. Appl. Meteor. Climatol.* **48**, 1302–1316 (2009).

40. Allen, R. & Ziv, A. Application of real time gps to earthquake early warning. *Geophys. Res. Lett.* **38**, 1–7 (2011).

41. Psimoulis, P. *et al.* Detection of seismic events using GPS network records: Case study Tohoku 2011 earthquake. In *IAG 2nd Nottingham GPS conference (9–10th september 2013) proceedings*, (2013).

42. Melgar, D., Bock, Y. & Crowell, B. W. Real-time centroid moment tensor determination for large earthquakes from local and regional displacement records. *Geophys. J. Int.* **188**, 703–718 (2012).

43. O'Toole, T., Valentine, A. & Woodhouse, J. Centroidmoment tensor inversions using highrate GPS waveforms. *Geophys. J. Int.* **191**, 257–270 (2012).

44. O'Toole, T., Valentine, A. & Woodhouse, J. Earthquake source parameters from GPS-measured static displacements with potential for real-time application. *Geophys. Res. Lett.* **40**, 60–65 (2013).

45. Wang, J., Huang, D. & Chang, S. Assessment of seismic hazard associated with the Meishan fault in Central Taiwan. *Bull. Eng. Geol. Environ.* **72**, 249–256 (2013).

46. Dalguer, L. A., Miyake, H., Day, S. M. & Irikura, K. Surface Rupturing and Buried Dynamic-Rupture Models Calibrated with Statistical Observations of Past Earthquakes. *Bull. Seismol. Soc. Am.* **98**, 1147–1161 (2008).

47. Pollitz, F., Nyst, M., Nishimura, T. & Thatcher, W. Inference of postseismic deformation mechanisms of the 1923 Kanto earthquake, Japan. *J. Geophys. Res.* **111**, 1–14 (2006).

48. Pollitz, F. *et al.* Viscoelastic-cycle model of interseismic deformation in the northwestern United States. *Geophys. J. Int.* **181**, 665–696 (2010).

49. Toda, S. & Stein, R. S. Response of the San Andreas Fault to the 1983 Coalinga-Nuez Earthquakes: An Application of Interaction-based Probabilities for Parkfield. *J. Geophys. Res.* **107**, ESE 6-1 ESE 6-16 (2002).

50. Gallovic, F., Käser, M., Burjánek, J. & Papaioannou, C. Three-dimensional modeling of the near-fault ground motions with non-planar rupture models and topography: Case of the 2004 Parkfield earthquake. *J. Geophys. Res.* **115**, 1–17 (2010).

51. Wald, D. & Heaton, T. Spatial and temporal distribution of slip for the 1992 Landers, California, earthquake. *Bull. Seismol. Soc. Am.* **84**, 668–691 (1994).

52. Liu, P., Custodio, S. & Archuleta, R. Kinematic Inversion of the 2004 M 6.0 Parkfield Earthquake Including an Approximation to Site Effects. *Bull. Seismol. Soc. Am.* **96**, S143–S158 (2006).

53. Kim, A. & Dreger, D. S. Rupture process of the 2004 Parkfield earthquake from near-fault seismic waveform and geodetic records. *J. Geophys. Res.* **113**, 1–16 (2008).

54. Page, M., S, C., Archuleta, R. & Carlson, J. Constraining earthquake source inversions with GPS data: 1. Resolution-based removal of artifacts. *J. Geophys. Res.* **114**, 1–13 (2009).

55. Custódio, S., Page, M. & Archuleta, R. Constraining earthquake source inversions with GPS data: 2. A two-step approach to combine seismic and geodetic data sets. *J. Geophys. Res.* **114**, 1–20 (2009).

56. Cirella, A., Piatanesi, A., Tinti, E., Chini, M. & Cocco, M. Complexity of the rupture process during the 2009 l'aquila, italy, earthquake. *Geophys. J. Int.* **190**, 607–621 (2012).

57. Ziv, A. Inference of coseismic slip via joint inversion of GPS and aftershock data: The 2004 Parkfield example. *J. Geophys. Res.* **117**, 1–7 (2012).

58. Twardzik, C., Madariaga, R., Das, S. & Custodio, S. Robust features of the source process for the 2004 Parkfield, California, earthquake from strong-motion seismograms. *Geophys. J. Int.* **191**, 1245–1254 (2012).

59. Anil-Bayrak, N. & Beresnev, I. Fault Slip Velocities Inferred from the Spectra of Ground Motions. *Bull. Seismol. Soc. Am.* **99**, 876–883 (2009).

60. Hartzell, S. H. & Heaton, T. H. Inversion of strong ground motion and teleseismic waveform data for the fault rupture history of the 1979 Imperial Valley, California, earthquake. *Bull. Seismol. Soc. Am.* **73**, 1553–1583 (1983).

61. Le Pichon, X., Kreemer, C. & Chamot-Rooke, N. Asymmetry in elastic properties and the evolution of large continental strike-slip faults. *J. Geophys. Res.* **110**, 1–11 (2005).

62. Jolivet, R., Bürgmann, R. & Houlié, N. Geodetic exploration of the elastic properties across and within the northern San Andreas fault zone. *Earth Planet. Sc. Lett.* **288**, 126–131 (2009).

63. Thurber, C. *et al.* Three-dimensional compressional wavespeed model, earthquake relocations, and focal mechanisms for the Parkfield, California, region. *Bull. Seismol. Soc. Am.* **96**, S38–S49 (2006).

64. Johnson, K., Bürgmann, R. & Larson, K. Frictional Properties on the San Andreas Fault Near Parkfield, California Inferred from Models of Afterslip Following the 2004 Earthquake. *Bull. Seismol. Soc. Am.* **96**, S321–S338 (2006).

65. Murray, J. & Langbein, J. Slip on the San Andreas Fault at Parkfield, California, over Two Earthquake Cycles, and the Implications for Seismic Hazard. *Bull. Seismol. Soc. Am.* **96**, S283–S303 (2006).

66. King, R. & Bock, Y. *Documentation of the GAMIT software.* MIT/SIO, (2006).

67. Langbein, J. *et al.* Preliminary Report on the 28 September 2004, M 6.0 Parkfield, California Earthquake. *Seis. Res. Lett.* **76**, 10–26 (2005).

68. Okada, Y. Internal deformation due to shear and tensile faults in a half-space. *Bull. Seis. Soc. Am.* **82**, 1018–1040 (1992).

69. Wright, T. *et al.* Source parameters of the 1 October 1995 Dinar (Turkey) earthquake from SAR interferometry and seismic bodywave modelling. *Earth Planet. Sc. Lett.* **172**, 23–37 (1999).

70. Goldstein, P., Dodge, D., Firpo, M. & Minner, L. SAC2000: Signal processing and analysis tools for seismologists and engineers. In *The IASPEI International Handbook of Earthquake and Engineering Seismology.* Academic Press, (2003).

71. Boore, D. M. Analog-to-Digital Conversion as a Source of Drifts in Displacements Derived from Digital Recordings of Ground Acceleration. *Bull. Seismol. Soc. Am.* **93**, 2017–2024 (2003).

72. Butterworth, S. On the Theory of Filter Amplifiers. *Wireless Eng.* **7**, 536–541 (1930).

73. Rhie, J., Dreger, D., Murray, M. & Houlié, N. Peak ground velocity ShakeMaps derived from geodetic slip models. *Geophys. J. Int.* **179**, 1105–1112 (2009).

74. Dreger, D., Hurtado, G., Chopra, A. & Larsen, S. Near-field across-fault seismic ground motions. *Bull. Seismol. Soc. Am.* **101**, 202–221 (2011).

75. Thurber, C., Brocher, T. M., Zhang, H. & Langenheim, V. Three-Dimensional P-wave Velocity Model for the San Francisco Bay Region, California. *J. Geophys. Res.* **112**, 1–19 (2007).

76. Dreger, D. & Kaverina, A. Seismic Remote Sensing for the Earthquake Source Process and Near-Source Strong Shaking: A Case Study of the October 16, 1999 Hector Mine Earthquake. *Geophys. Res. Lett.* **27**, 1941–1944 (2000).

77. Dreger, D. & Romanowicz, B. Source characteristics of events in the San Francisco Bay Region. *U. S. Geol. Surv. Open File Rep.* **94**, 301–309 (1994).

78. Liu, P., Custódio, S. & Archuleta, R. J. Kinematic Inversion of the 2004 M 6.0 Parkfield Earthquake Including an Approximation to Site Effects. *Bull. Seismol. Soc. Am.* **96**, S143–S158 (2006).

79. Allmann, B. & Shearer, P. A High-Frequency Secondary Event During the 2004 Parkfield Earthquake. *Science* **318**, 1279–1283 (2007).

80. Johanson, I. A., Fielding, E. J., Rolandone, F. & Bürgmann, R. Coseismic and Postseismic Slip of the 2004 Parkfield Earthquake from Space-Geodetic Data. *Bull. Seismol. Soc. Am.* **96**, S269–S282 (2006).

81. Bennington, N., Thurber, C., Feigl, K. & Murray-Moraleda, J. Aftershock Distribution as a Constraint on the Geodetic Model of Coseismic Slip for the 2004 Parkfield Earthquake. *Pure Appl. Geophys.* **168**, 1552–1565 (2011).

82. Rymer, M. J. *et al.* Surface Fault Slip Associated with the 2004 Parkfield, California, Earthquake. *Bull. Seismol. Soc. Am.* **96**, S11–S27 (2006).

83. Bruhat, L., Barbot, S. & Avouac, J.-P. Evidence for postseismic deformation of the lower crust following the 2004 Mw6.0 Parkfield earthquake. *J. Geophys. Res.* **116**, 1–10 (2011).

84. Langbein, J., Murray, J. R. & Snyder, H. A. Coseismic and initial postseismic deformation from the 2004 Parkfield, California, earthquake, observed by global positioning system, electronic distance meter, creepmeters, and borehole strainmeters: Bulletin of the Seismological Society of America, **96**, S304–S320, doi: 10.1785/0120050823. (2006).

85. Thurber, C. *et al.* Fine-scale structure of the San Andreas fault zone and location of the SAFOD target earthquakes. *Geophys. Res. Lett.* **31**, 1–7 (2004).

Acknowledgments

Author contributions

N.H. initial idea, conception and writing; N.H. and D.D. wrote the text. A.K. completed the first set of inversion.

Additional information